Stanford Exploration Project, Report 115, May 22, 2004, pages 399–411

Teleseismic imaging with wave equation migration

Charles K. Wilson, Jeff Shragge, and Brad Artman[1]

ABSTRACT

Images of the lithosphere from three-component seismic arrays recording wavefields generated by teleseismic earthquakes (30°- 90° epicentral distance) reveal important aspects of lithospheric structure. Unfortunately, interpretation of these images remains ambiguous due to improper reflector mapping and amplitude restoration. We introduce the shot-profile representation of wave equation migration as a novel way to cast the teleseismic imaging problem. We show results from two synthetic datasets using both forward- and backscattered modes to demonstrate the strength of this imaging scheme. To demonstrate the techniques effictiveness with real data, we present preliminary images from the forward-scattered P-to-S mode from data collected across the Proterozoic Cheyenne suture near Laramie, Wyoming.

INTRODUCTION

Deployments of regionally extensive seismic arrays in the last decade have provided earthquake data that afford images of the lithosphere at scales hitherto unattainable (Dueker and Sheehan, 1998; Rondenay et al., 2001; Poppeliers and Pavlis, 2003; Wilson et al., 2003). Attesting to their importance, these images now play a crucial role in improving our understanding of past and present processes of tectonic evolution. The next decade, owing to the EARTHSCOPE[2] program and the associated US-ARRAY, will see a dramatic increase in the volume of three-component broad-band seismic data available for imaging the North American lithosphere. However, to fully exploit this opportunity current lithospheric imaging practice must be improved.

Most teleseismic imaging experiments use forward-scattered P-to-S converted waves isolated using receiver function analysis (Phinney, 1964; Langston, 1977). The reasons for concentrating only on this phase are mainly historical. Before the use of receiver arrays became commonplace in teleseismic imaging, only data from sparsely distributed three-component stations were available. Seismologists interested in structure beneath a seismic station were forced to use scattered phases that could be identified and isolated from a single set of three-component seismograms. One easily identified phase is horizontally polarized shear waves converted from lithospheric discontinuities by nearly vertically incident teleseismic P waves; However, identifying backscattered phases (e.g. free surface multiples) requires the use of

[1]**email:** wilsonck@sep.stanford, brad@sep.stanford.edu, jeff@sep.stanford.edu

[2]http://www.earthscope.org

moveout variations instead of polarization. For a single station, there is no moveout of scattered phases without several teleseismic sources from a variety of distances thereby making use of other scattered phases nearly impossible.

Contemporaaneously, the introduction of spatially extensive three-component seismic arrays, earthquake seismologists began adapting imaging practices of exploration seismology to produce images of the crust and mantle with teleseismic waves. Initial work in teleseismic imaging used simple processing flows involving linear moveout corrections combined with common conversion point stacking (Dueker and Sheehan, 1998). Later efforts attempted to adopt Kirchoff imaging schemes to produce images of the Cascadia subduction zone (Rondenay et al., 2001) and an Archean continental suture in Southwestern Wyoming (Sheehan et al., 2000). Rondenay et al. (2001) and more recent work by Aprea et al. (2002) clearly demonstrated the utility of backscattered phases in lithospheric imaging and fomenting a new direction for future teleseismic imaging research.

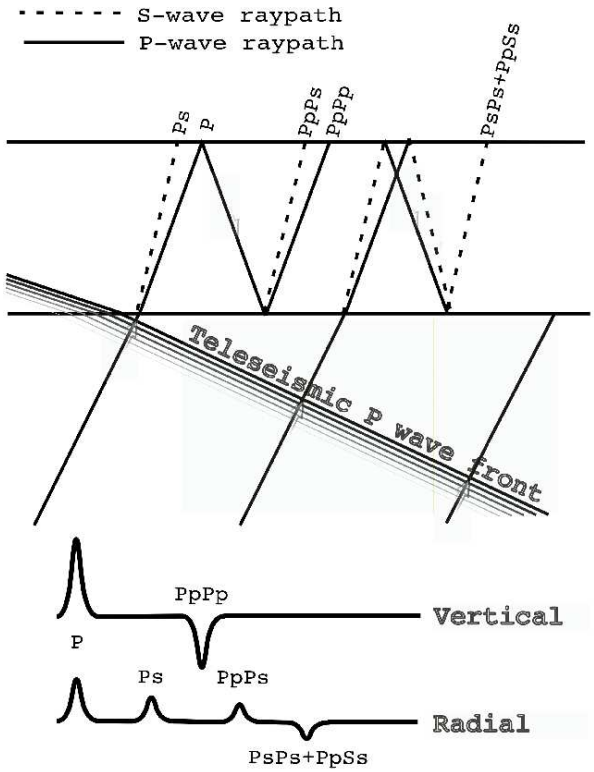

Figure 1: Ray paths of forward and backscattered phases generated by an impinging teleseismic P wave front. Solid lines mark P ray paths with S rays marked by dashed lines. Uppercase letters denote downgoing phases with lowercase letters symbolizing upgoing phases. The idealized vertical and radial seismograms indicate the approximate arrival and amplitude relationships for some of the arrivals in the ray diagram above. The diagram demonstrates the natural separation of P and S phases from near vertically incident waves onto the vertical and horizontal components. charlie1-RFcart [NR]

There are clear advantages of wave equation imaging over Kirchoff in exploration seismology. Most likely these advantages remain valid even in the modified geometry of teleseismic sources and receivers (Shragge and Artman, 2003) where lateral velocity heterogeneity is often encountered (e.g. in the presence of partial melt or along large offset strike-slip faults). The shot-profile formulation of wave-equation migration provides a framework in which to cast the teleseismic imaging experiment that allows the incorporation of other scattering modes besides forward-scattered P-to-S. In this paper, we demonstrate its utility for several scattered modes produced by a teleseismic P wavefield impinging on two simple (yet realistic) synthetic crustal models. We also show images from migrated forward-scattered P-to-S converted phases from a dense profile across the Cheyenne suture near Laramie, Wyoming and compare

them to images obtained using conventional receiver function stacking techniques (Dueker and Yuan, 2004).

SOURCE-RECEIVER GEOMETRY OF TELESEISMIC IMAGING

By definition, teleseismic earthquake sources originate at a great distance from the receiver array and have ray turning points in the middle-to-lower mantle (>400 km depth). As a result, source wavefields are nearly vertically incident, planar wavefronts arriving beneath the receiver array. Thus, the recorded wavefield is a combination of the source along with the P and S scattered modes generated by the incoming plane wave. Figure 1 shows a schematic example of the teleseismic wavefield and the modes we use for imaging. The synthetic teleseismic wavefield shown in Figure 2 illustrates the combined source and receiver wavefield recorded by the surface array. The first arrival is the source wavelet followed by the forward-scattered P-to-S conversion seen near 13 seconds on the radial and the backscattered P-to-P phase on the vertical near 20 seconds. As demonstrated by the synthetic seismograms, the

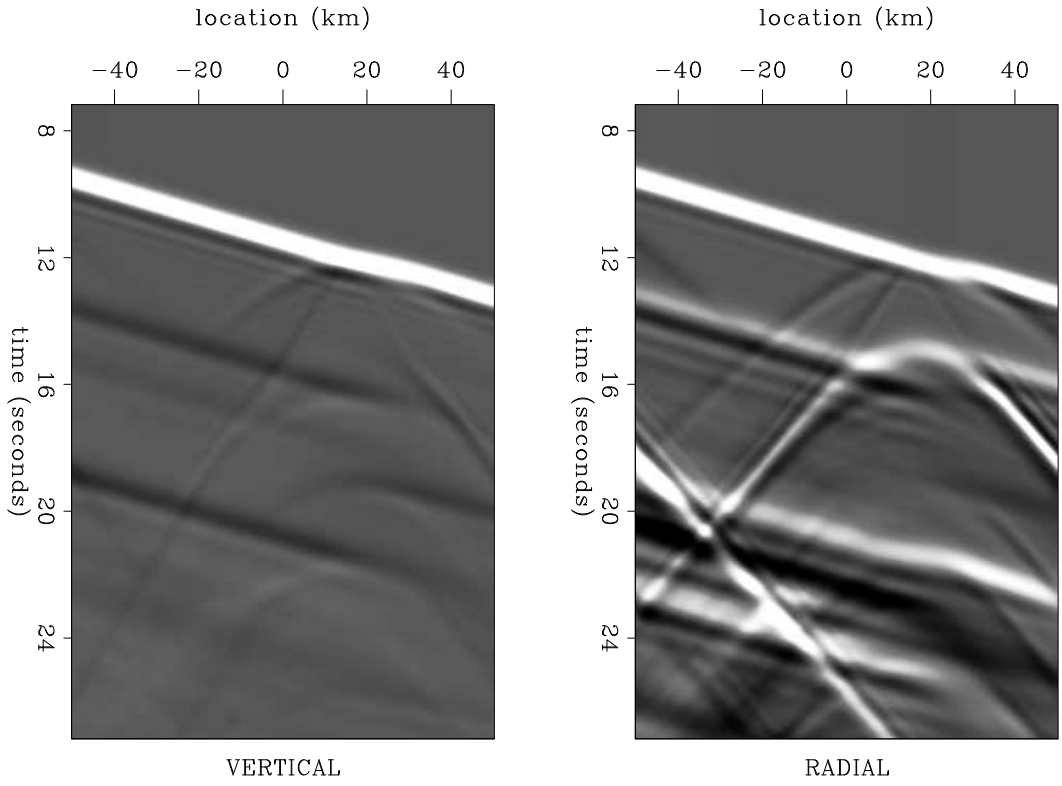

Figure 2: Synthetic seismograms calculated for a crustal model with an 8 km Moho offset. charlie1-stepSYNTH [CR]

plane-wave source creates secondary sources in the form of free surface reflections. These reflections retain a significant amount of energy and produce subsurface reflections often several times larger in amplitude than their forward-scattered counterparts. In theory,free-surface multiples provide additional information that may be used in a more traditional up-

going/downgoing wavefield framework. However, without a means to discriminate between forward and backscattered phases propagating as both P and S waves we may expect a significant amount of contamination between modes. Component rotation from [V,N,E] into the [P,Sv,Sh] system using the free-surface transfer matrix (Kennett, 1991) allows us to identify phases based on polarization direction. Cross-contamination by modes not traveling nearly parallel to the predicted source wave propagation direction still occurs.

WHY SHOT-PROFILE MIGRATION?

The primary advantage of the shot-profile formulation of wave equation migration for teleseismic imaging comes from the ability to separate the source and receiver wavefields for independent propagation during propagation. Shot-profile migration separates the total wavefield into source and receiver wavefields that are each propagated separately (by Fourier-domain multiplication) with the appropriate single square root (SSR) operators (Claerbout, 1995).

$$\begin{aligned} S_s(\omega, k_x, z+\Delta z) &= S_s(\omega, k_x, z) e^{-ik_z \Delta z} \\ R_s(\omega, k_x, z+\Delta z) &= R_s(\omega, k_x, z) e^{ik_z \Delta z}. \end{aligned} \tag{1}$$

Here S_s is the source wavefield for a recorded teleseismic event s and R_s represents the receiver wavefield. The negative sign on the single square root operator exponent applied to the source wavefield denotes an initially downgoing wavefield. To represent source and receiver wavefields traveling in the same (upgoing) direction we apply a positive exponent to the single square root operator of each wavefield. The strength of this method comes from the implicit assignment of source and receiver wavefield mode (P or S waves) and propagation direction based on the choice of velocity model and operator exponent, respectively. Following the passive seismic methodology developed previously by Claerbout (1968), we attempt to exploit this direct observation of the source wavefield thereby minimizing the amount of prior assumptions and preprocessing (Artman and Shragge, 2003). Single components of our recorded wavefield may be treated as a source representation with the particular component chosen according to the scattering mode of interest. Table 1 shows the sign and velocity model used to propagate both the source and receiver wavefields for several possible scattering modes.

After propagation of the wavefields, image computation results from a frequency summation of the deconvolution at each depth.

$$\mathbf{I}(x,z) = \sum_{\omega} \frac{\mathbf{R_s}(x,z,\omega)\mathbf{S_s}^*(x,z,\omega,)}{\mathbf{S_s}(x,z,\omega)\mathbf{S_s}^*(x,z,\omega) + \varepsilon^2} \tag{2}$$

After computing individual images from each scattering mode for individual earthquakes, we create composite images for each scattering mode by summing images from all recorded earthquakes. We produce a final image by summing all images produced by all scattering modes.

Mode	Scattering Mode	Source Prop. Dir.	S. Velocity	R. Velocity	Rec. Component
1	FS P-P	-	P	P	$\overline{P}$
2	FS P-S	-	P	S	$\overline{SV}$
3	BS P-P	+	P	P	$\overline{P}$
4	BS P-S	+	P	S	$\overline{SV}$
5	BS S-P	+	S	P	$\overline{P}$
6	BS S-S	+	S	S	$\overline{SV}$
7	BS S-S	+	S	S	$\overline{SH}$

Table 1: Table listing of the scattering modes, propagation velocity, and propagaton direction for each source and receiver wavefield for different scattering modes.

SYNTHETIC TESTING

In this section we show the results of migration of modes 2 through 4 from table 1. The synthetic data consists of 16 plane waves at angles of incidence between $-30°$ and $30°$ propagated through two crustal models: one containing an 8 km offset in the Moho near 30 km depth and another containing a dipping Moho (Figure 3). Figure 2 and Figure 4 show vertical and radial seismograms from the offset and dipping Moho models, respectively. Notice the clear diffracted arrival generated by the Moho offset in Figure 2 that are not present in Figure 4. Also, interesting is the focusing that occurs at the ramp due to the apparent increase of incidence angle due to the structural dip. Contamination from side reflections later in time prohibits our ability to use some later arriving backscattered phases.

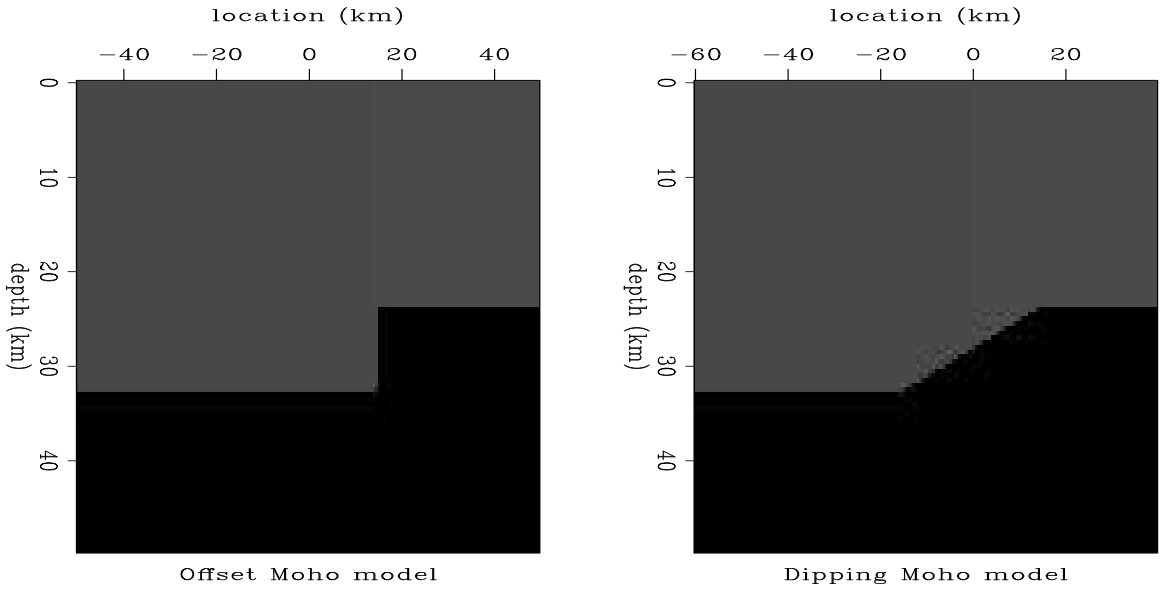

Figure 3: Velocity models used to generate finite-difference synthetic seismograms. charlie1-Vmod [CR]

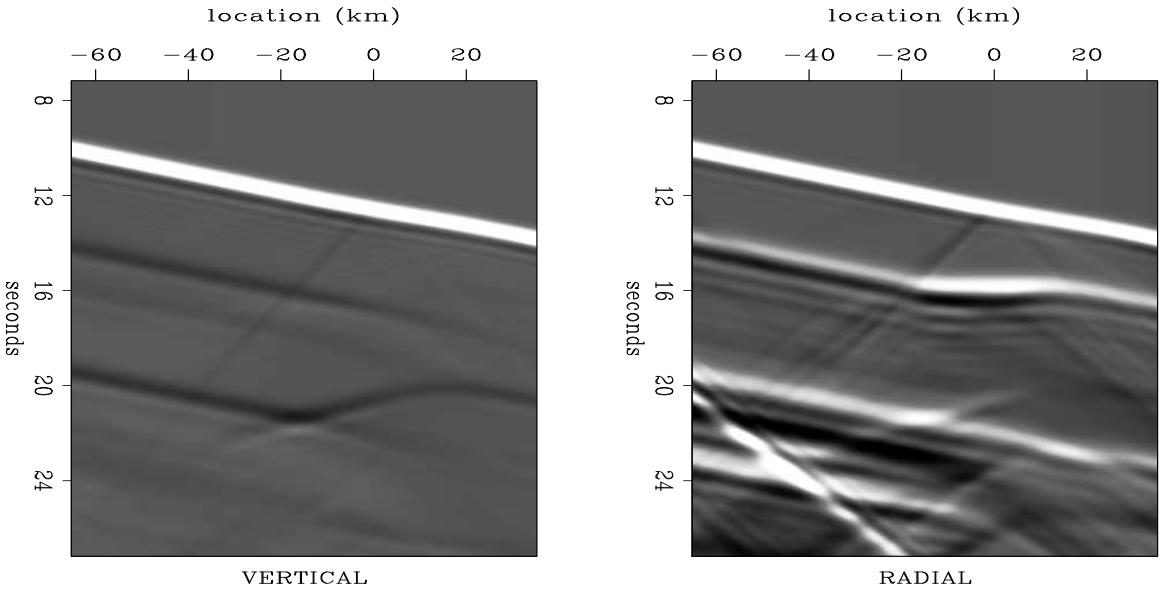

Figure 4: Synthetic seismograms calculated for a crustal model with a dipping Moho. charlie1-dipSYNTH [CR]

We use a receiver spacing of 0.5 km to represent a densely sampled teleseismic experiment. In practice, this sampling is impractical but is necessary here to concentrate on the limitations of the procedure without adding complexity due to wavefield aliasing. Stacked images from individual modes and all modes are shown in the next sections.

Figure 5 shows the images created with the forward-scattered P-to-S phase for both synthetic models. Both structures are clearly visible although they appear blurred. The low frequency image results from the fact that the wavefields propagate in the same direction and therefore remain correlated over more imaging depths. We show images created with backscattered P-to-P for both synthetic models in Figure 6. Both structures appear better resolved. The high amplitude shallow structure results from erroneously migrated cross-contamination from the forward-scattered P-to-S phase. This indicates cross-contamination may render interpretation of shallow structures difficult. Figure 7 created using backscattered P-to-S conversion also appears heavily contaminated by other phases. This is most apparent in the Moho offset synthetic model (top panel) where the Moho appears to stretch completely across the image. Combining all images reduces the contamination from other phases and sharpens the real crustal features. However, a significant shallow artifact still remains in both images.

APPLICATION TO DATA RECORDED BY THE LARAMIE BROAD-BAND ARRAY

The Laramie broad-band array which consisted of 30 CMG-40T three-component seismometers spaced between one and two kilometers apart, recorded continuously for 8 months in 2000-2001. The focus of the project was to image the Proterozoic Cheyenne Suture represent-

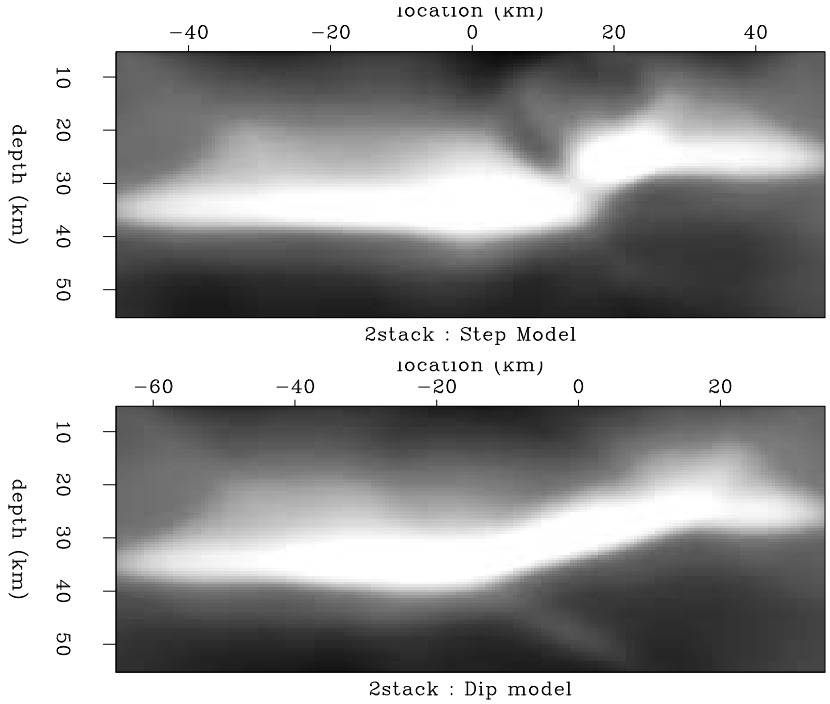

Figure 5: Migrated image of all synthetic events computed using forward-scattered P-to-S waves for the Moho offset model (top) and the and the model with the dipping Moho (bottom). charlie1-2stack [CR]

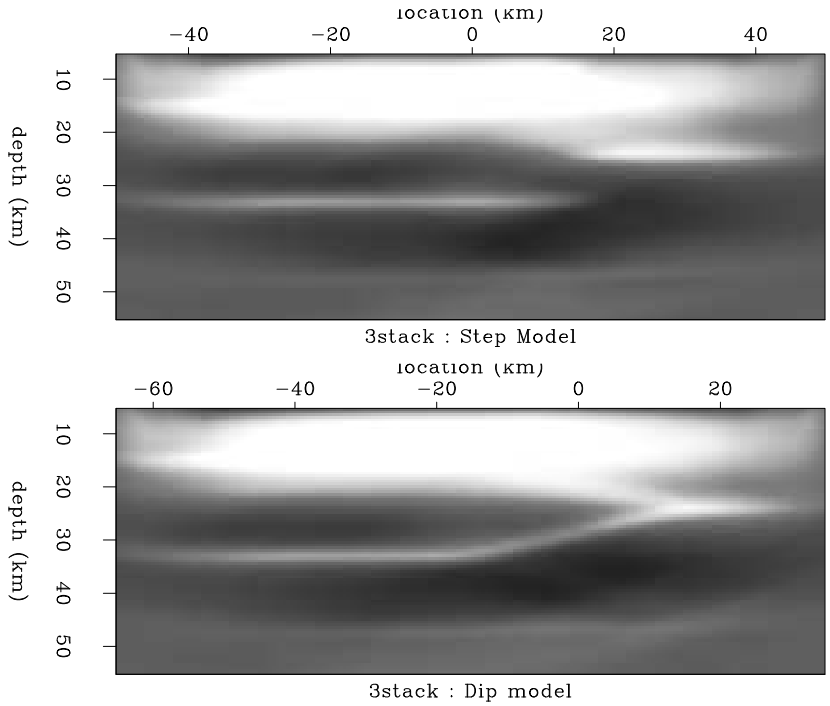

Figure 6: Migrated image of all synthetic events computed using backscattered P-to-P waves for the Moho offset model (top) and the and the model with the dipping Moho (bottom). charlie1-3stack [CR]

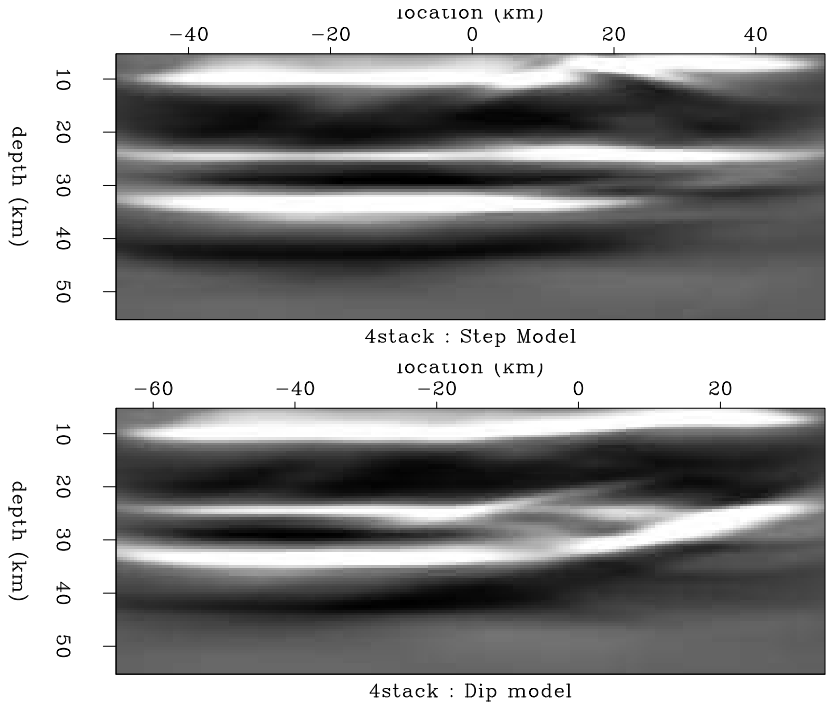

Figure 7: Migrated image of all synthetic events computed using backscattered P-to-S waves for the Moho offset model (top) and the and the model with the dipping Moho (bottom). charlie1-4stack [CR]

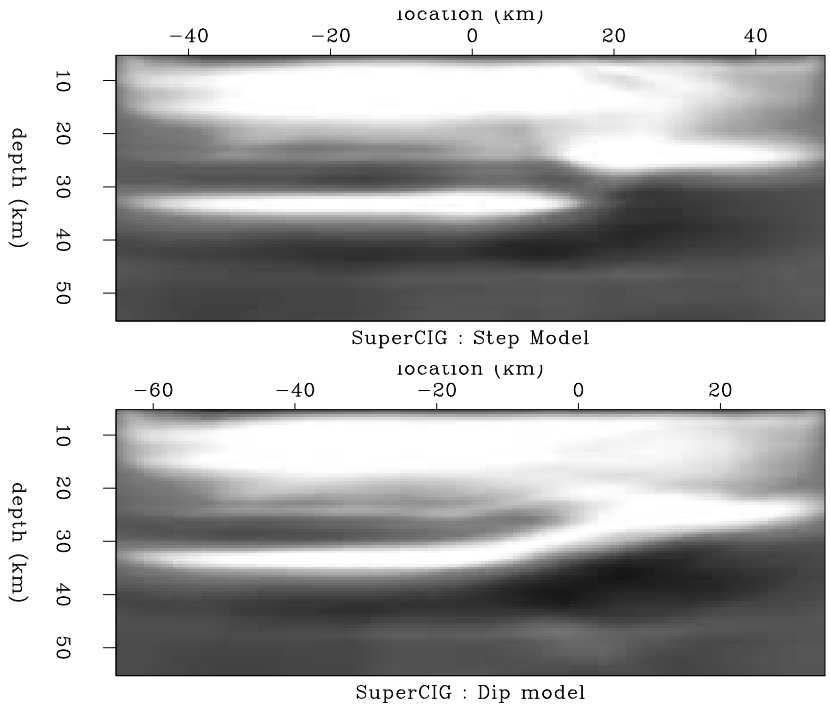

Figure 8: Migrated image of all synthetic events and all modes shown previously for the Moho offset model (top) and the dipping Moho model (bottom). charlie1-SuperCIG [CR]

ing a nearly 2 billion years old continental collision. The array trending northwest-southeast, straddled the northern edge of the suture. Dueker and Yuan (2004) produced an image us-

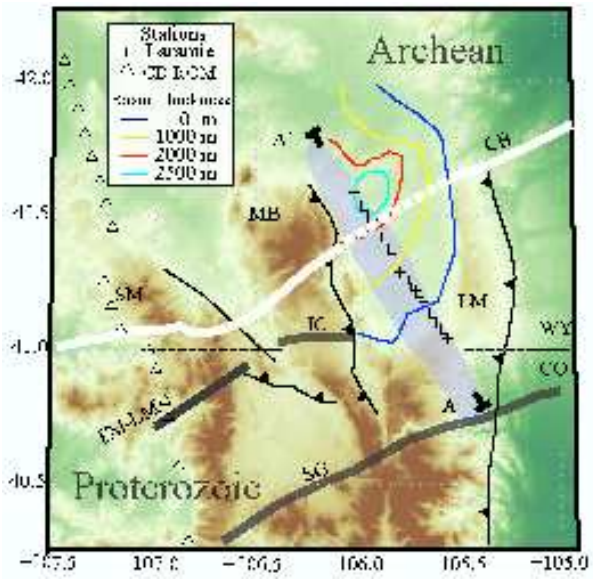

Figure 9: The X's represent the stations associated with the Laramie array. Note large thickness of the Laramie basin shown by the contours. The sampling area of the teleseismic dataset at 40 km depth is shown as the gray ellipsoidal area. The Cheyenne belt suture (CB) surface expression is shows as the thick white line (dotted where inferred). Major NE-trending shear zones are marked as thick dark lines and denoted as: FM, Farwell Mountain; SG, Skin Creek Gulch; IC, Illinois Creek. Surrounding mountains that expose the basement are labeled as: SM, Sierra Madre; MB, Medicine Bow; LM, Laramie Mts. Image modified from Dueker and Yuan, 2004. charlie1-map [NR]

ing receiver function analysis where the vertical component is treated as the source function and deconvolved from the radial component. Application of a linear moveout operator to the processed seismograms followed by common conversion point stacking produced the image shown in Figure 10. Important features of this image include the mid-crustal reflector near 20 km depth and the Moho which is interpreted to be near 40 km depth across the line. A second feature dips down below the Moho to the north to a depth of 60 km. Dueker and Yuan (2004) interpret this feature to be a sliver of crust thrust underneath the Wyoming craton during collision.

We have created a migrated image of the forward-scattered P-to-S phase using the same data for comparison to the receiver function image. The results are consistent in many parts of the image including the feature near 20 km depth and the dipping feature between 40 and 60 km depth. However the feature interpreted to be the Moho in the north is absent from our image casting doubt on the previous interpretation. The migrated image appears to be very noisy and low frequency. A different source representation, perhaps as a band limited plane wave, and the incorporation of backscattered phases would improve the image.

CONCLUSIONS

We have demonstrated the potential of the wave equation based shot-profile migration developed by Artman and Shragge (2003) for imaging with the teleseismic wavefield using two

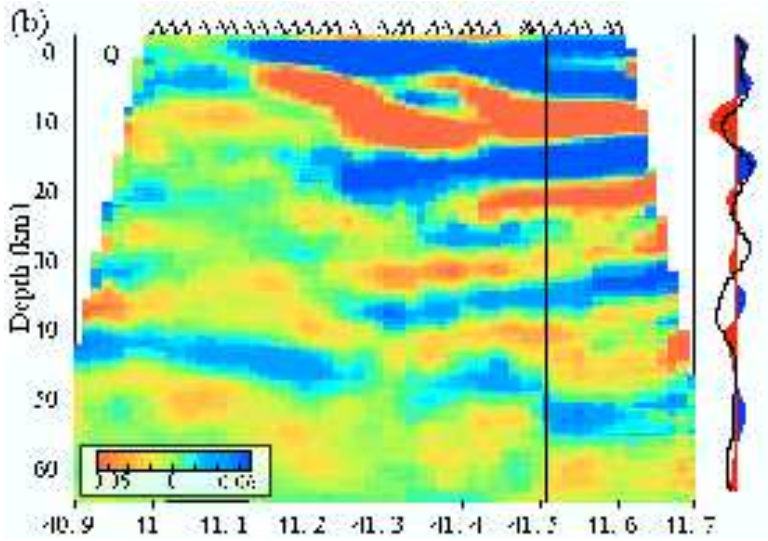

Figure 10: Common conversion point stacked image using receiver function analysis on data recorded by the Laramie Broad-Band Array. charlie1-Laramie_Xsect [NR]

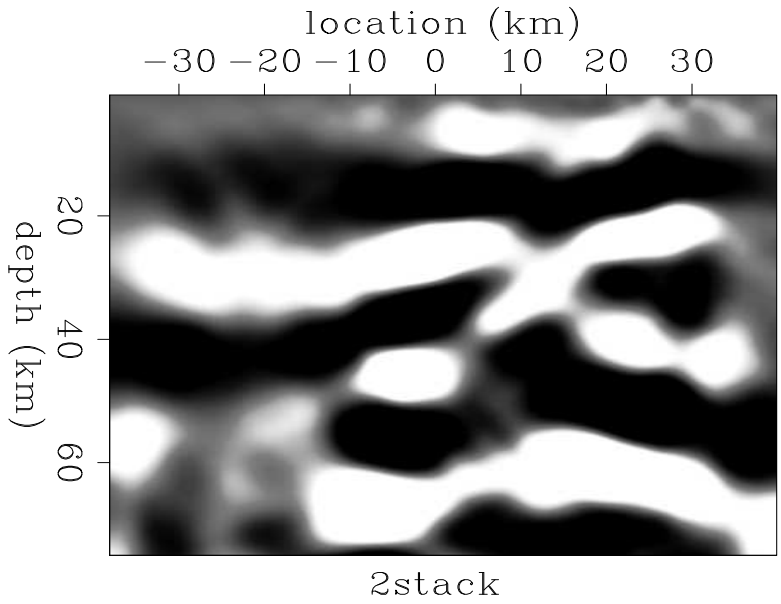

Figure 11: Migrated image of all events computed using forward-scattered P-to-S converted waves recorded by the Laramie Broad-Band Array. charlie1-2stack_LARAMIE [CR]

synthetic datasets. In addition, preliminary images produced with the forward-scattered P-to-S mode correlate well with previous methodology. The images may be enhanced with better source wavefield modeling and wavefield interpolation prior to processing. Other improvements could be made by imaging each scatterig mode after multiple and/or primary suppression or simultaneously inverting the entire wavefield to solve for a single earth model defined by all scattering modes (e.g. simultaneous multiple and primary migration).

ACKNOWLEDGMENTS

The first author would like to thank everyone in SEP for their patience and assistance while becoming accustomed to the SEP environment. We also thank Hy Yuan and Ken Dueker for use of their P wave velocity model and also the map and images from the Laramie experiment.

REFERENCES

Aprea, C. M., Hildebrand, S., Fehler, M., Steck, L., Baldridge, W. S., Roberts, P., Thurber, C. H., and Lutter, W. J., 2002, Three-dimensional Kirchhoff migration: Imaging of the Jemez volcanic field using teleseismic data: J. Geophys. Res., **107**, no. B10, art. no.–2247.

Artman, B. W., and Shragge, J. C., 2003, Passive seismic imaging: EOS Trans. AGU, 84(46), Fall Meet. Suppl., **Abstract S11E-0334**.

Claerbout, J. F., 1968, Synthesis of a layered medium from its acoustic transmission response: Geophysics, **33**, no. 02, 264–269.

Claerbout, J. F., 1995, Basic Earth Imaging: Stanford Exploration Project, `http://sepwww.stanford.edu/sep/prof/`.

Dueker, K. G., and Sheehan, A. F., 1998, Mantle discontinuity structure beneath the Colorado Rocky Mountains and High Plains: J. Geophys. Res., **103**, no. B4, 7153–7169.

Dueker, K. G., and Yuan, H., 2004, Crustal imbrication across the Archean-Proterozoic Cheyenne belt suture from the Laramie broad-band seismic array in Southeast Wyoming, U.S.A.: Submitted to Geophysical Research Letters.

Kennett, B. L. N., 1991, The removal of free surface interactions from three-component seismogr ams: Geophys. J. Int., **104**, 153–163.

Langston, C. A., 1977, Effect of planar dipping structure on source and receiver responses for constant ray parameter: Bull. Seismol. Soc. Amer., **67**, no. 4, 1029–1050.

Phinney, R. A., 1964, Structure of the earth's crust from spectral behavior of long-period body waves: J. Geophys. Res., **69**, no. 14, 2997–3017.

Poppeliers, C., and Pavlis, G. L., 2003, Three-dimensional, prestack, plane wave migration of teleseismic p-to-s converted phases: 2. stacking multiple events: J. Geophys. Res., **108**, no. B5, art. no.–1583.

Rondenay, S., Bostock, M. G., and Shragge, J., 2001, Multiparameter two-dimensional inversion of scattered teleseismic body waves 3. application to the cascadia 1993 data set: J. Geophys. Res., **106**, no. B12, 30795–30807.

Sheehan, A. F., Shearer, P. M., Gilbert, H. J., and Dueker, K. G., 2000, Seismic migration processing of p-sv converted phases for mantle discontinuity structure beneath the snake river plain, western united states: J. Geophys. Res., **105**, no. B8, 19055–19065.

Shragge, J. C., and Artman, B. W., 2003, Wave-equation imaging of teleseismic body-wave coda: EOS Trans. AGU, 84(46), Fall Meet. Suppl., **Abstract S11E-0335**.

Wilson, C. K., Jones, C. H., and Gilbert, H. J., 2003, Single-chamber silicic magma system inferred from shear wave discontinuities of the crust and uppermost mantle, Coso geothermal area, California: J. Geophys. Res., **108**, no. B5, art. no.–2226.